Optimized Design of Piezoelectric Flap Actuators for Active Flow Control

Jose Mathew,* Qi Song,* Bhavani V. Sankar,† Mark Sheplak,‡ and Louis N. Cattafesta III‡
University of Florida, Gainesville, Florida 32611-6250

Piezoelectric flap actuators are often used in active flow-control applications. However, effective design tools are lacking in the flow-control community. This paper discusses theoretical modeling, experimental validation, and optimal design of piezoelectric unimorph and bimorph flap actuators. First, two different finite element models are described. One is a simple beam model that assumes a perfect bond exists between the piezoelectric patch and the shim, whereas the second incorporates a linear elastic shear element for the bond layer. These models are then used to predict the magnitude of the dc response (tip displacement per unit applied voltage) and the natural frequency (a measure of the bandwidth) of these actuators. Next, an approximate analytical model is developed to facilitate design optimization. The models are compared with experimental data obtained from a parametric study in which 10 otherwise identical unimorph piezoelectric actuators with varying piezoelectric patches are fabricated and characterized using a laser displacement sensor. All models produce estimates that are accurate to within ±15% and ±10% for the dc response and natural frequency, respectively. The analytical model is also extended to bimorph actuators. Finally, a general design optimization procedure is presented, and representative results are provided.

Introduction

ACTIVE flow control is a field that has gained significant attention due to recent advances in the understanding of the role of coherent flow structures in the dynamics of turbulent shear flows. Piezoelectric actuators are widely used in flow-control applications due to their ability to introduce controlled disturbances into such flows. These actuators are attractive because they are inexpensive, compact, easy to build, and consume small amounts of power. Typical applications, depicted in Fig. 1, include active control of separation [1], streamwise vortices and streaks in turbulent boundary layers [2], excitation of instabilities in free shear flow [3,4], and suppression of flow-induced cavity oscillations [5]. Each of these and similar publications emphasize the relevant fluid dynamics but largely ignore the modeling and design of the actuators for their respective applications.

The usual goal of an actuator model is to enable the design of a device that is optimized in some sense for a prescribed application. Typical requirements include maximizing the stroke over a prescribed bandwidth. A flat frequency response with minimal phase lag is a desirable characteristic when using actuator arrays, as shown in Fig. 1a, 1c, and 1d, to ensure prescribed phase differences between the array elements. These requirements emphasize the importance of a design methodology that properly accounts for the dynamic response of the actuator.

Although numerous models exist in the literature concerning the electromechanics of piezoelectric benders [6–8], a suitable optimal design methodology specifically suited for fluid dynamic applications does not. The contribution of the present work is the development of validated design tools for piezoelectric flaps or benders that can produce significant flow disturbances over a prescribed bandwidth. In particular, this paper critically evaluates

several finite element models of varying complexity and develops an analytical model of a piezoelectric "unimorph" actuator (a piezoelectric patch on one side of the beam) via a detailed parametric experimental study. The validated model is then generalized to the simpler "bimorph" actuator with a piezoelectric patch placed symmetrically on each side of the beam. A design optimization procedure is developed and illustrated by using the analytical model to maximize the tip displacement of the actuator at the maximum electric field strength for a prescribed bandwidth of operation.

Theoretical Modeling

Figure 2 shows a schematic of a piezoelectric unimorph actuator with a total shim length L_T, width b, and thickness t_s. A piezoelectric patch of length L_p, width b, and thickness t_p is bonded to the shim using an epoxy adhesive of thickness t_b. A small gap of length L_{gap} (<1 mm) is maintained between the clamp and the piezoelectric patch to reduce stress concentrations and to prevent an electrical short circuit during vibration. Upon application of an external voltage to the piezoelectric electrode, a bending moment is generated, and the actuator deflects in a direction determined by the orientation of the piezoelectric polarization vector with respect to the electric field.

To characterize piezoelectric actuators, a structural dynamics model is required that can accurately predict the frequency response of the actuators. Because flow-control applications of interest typically demand a large tip displacement, attention is restricted to the first bending mode only. Crawley and de Luis [6] showed that for maximum tip displacement in a bending configuration, the optimal location of the piezoelectric patch corresponds to the vicinity of maximum strain, i.e., near the clamp location. However, the choice of the size (t_p and L_p) of the patch is not so clear because larger patch sizes induce greater deflections but also affect the mass and stiffness of the structure and therefore influence its natural frequency. Another practical implementation issue that arises is the effect of the bond layer on the dynamics of the actuator. The bond layer that attaches the piezoelectric layer to the shim induces a shear lag and also adds to the damping of the system. Below, "perfect-bond" and "shear-lag" models, both of which use finite element methodologies, are used to calculate the frequency response of the actuators to an applied voltage.

*Graduate Research Assistant, Mechanical and Aerospace Engineering Department, 231 MAE-A. Student Member AIAA.

†Ebaugh Professor, Mechanical and Aerospace Engineering Department, 231 MAE-A. Associate Fellow AIAA.

‡Associate Professor, Mechanical and Aerospace Engineering Department, 231 MAE-A. Associate Fellow AIAA.
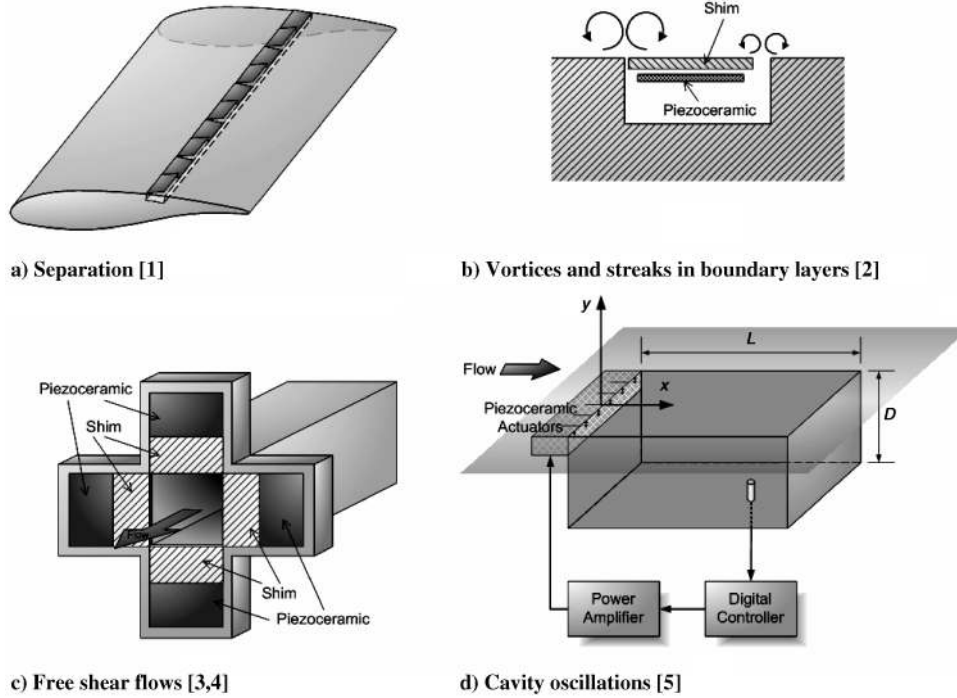
a) Separation [1]

b) Vortices and streaks in boundary layers [2]

c) Free shear flows [3,4]

d) Cavity oscillations [5]

Fig. 1 Sample active flow-control applications of piezoelectric flap actuators.
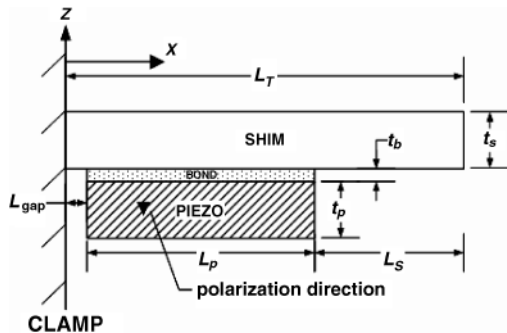

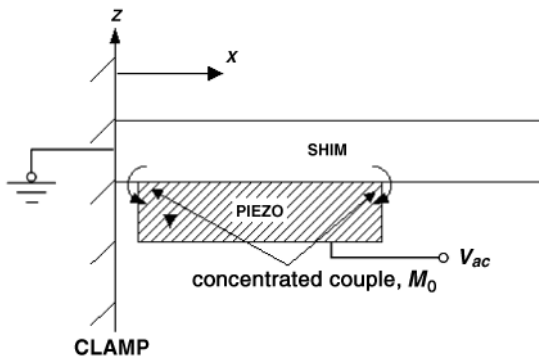**Fig. 2 Schematic of piezoelectric unimorph actuator model.**

Fig. 3 Schematic of perfect-bond model.

Perfect-Bond Model

A simple schematic of the perfect-bond model is shown in Fig. 3. This assumes an infinitely rigid bond exists between the piezoelectric patch and the shim, which implies that all strain applied to the bond by the piezoelectric layer is completely transmitted to the shim.

Crawley and de Luis [6] showed that a perfect bond between the piezoelectric patch and the shim leads to a concentrated couple or moment M_o at the edges of the piezoelectric patch, $x = L_{gap}$ and $x = L_{gap} + L_p$. As described in Cattafesta et al [7], the applied voltage for pure bending is related to M_o by

$$M_o = -\frac{1}{2} E_p d_{31} E_{field} b t_p (2c_2 - t_p) \tag{1}$$

where E_p is the elastic modulus of the piezoelectric patch, d_{31} is the piezoelectric modulus, and $E_{field} = V/t_p$ is the magnitude of the applied electric field due to an applied voltage V. The parameter c_2 is the location of the neutral axis in the composite region with respect to the bottom surface of the piezoelectric patch and can be obtained by equating the net axial force at any cross section along the actuator to zero [7].

A standard Euler–Bernoulli beam finite element model was developed to calculate the frequency response function for the piezoelectric actuators. The details of the finite element scheme are given in Cattafesta et al. [8]. The material properties of the actuators are summarized in Table 1.

Shear-Lag Model

The shear-lag model extends the perfect-bond model to the case where a viscoelastic bond layer of finite stiffness is used to attach the

Table 1 Piezoelectric actuator properties

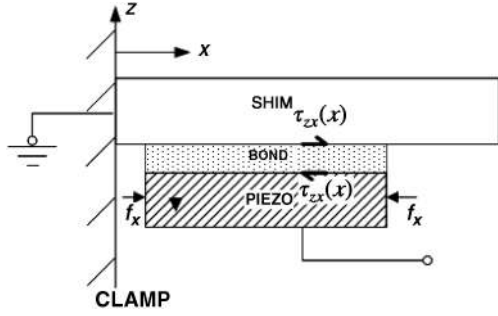| Property	AL-2024 (aluminum shim)	PZT-5H (piezoelectric material)	Eccobond 45 (adhesive)
Elastic modulus, GPa	73.3	62.0	0.398
Density, kg/m³	3290	7500	1060
Piezoelectric modulus, d_{31}, m/V	——	-274×10^{-12}	——
Shear modulus, GPa	——	——	0.148

Fig. 4 Schematic of shear-lag model.

shim to the piezoelectric layer. Such materials have an elastic part that stores energy and a viscous part that dissipates energy due to damping [9]. A schematic of the shear-lag model is shown in Fig. 4. Crawley and de Luis [6] showed that the maximum shear stress occurs near the edges of the bond layer, whereas the shear stress distribution is approximately zero elsewhere in the bond layer. The shear stress distribution also has opposite signs at the two edges of the bond layer. Because of the deformation of the piezoelectric layer induced by the application of an external electric field, a horizontal electromechanical force of magnitude $f_x = d_{31}E_{\text{field}}E_p A$ acts on the front and back faces of the piezoelectric region, where $A = bL_p$ is the cross-sectional area of the piezoelectric patch. A shear stress $\tau_{zx}(x)$ acts at the interface between the bond and the piezoelectric patch (and the bond and shim), as shown in Fig. 4. A free-body diagram of the piezoelectric layer reveals the relationship between the magnitudes of the net shear force f_x and $\tau_{zx}(x)$,

$$f_x = \int_0^{L_p/2} \tau_{zx}(x)b \, dx \qquad (2)$$

This horizontal electromechanical force induces a moment M_0 that is related to f_x by

$$f_x = \frac{-2L_p M_0}{(2c_2 - t_p)t_p} \qquad (3)$$

Thus, the actuator deflects or bends upon application of a voltage, and the direction of motion is determined by the orientation of the piezoelectric polarization vector with respect to the electric field. The net effect is a finite shear stress or shear lag, $\tau_{zx}(x) = G_b(\partial u/\partial z)$, that is induced in the bond layer due to the deformation of the piezoelectric layer, resulting in a decreased induced strain being transmitted to the shim. Here, u is the displacement in the x direction, and G_b is the shear modulus of the bond layer.

A finite element model, similar to the one used for the perfect-bond model, was developed. The solution procedure is similar to that of the perfect-bond model, and the details are given in Mathew et al. [10].

Analytical Model

To obtain the functional dependence of critical quantities such as dc response and natural frequency on the actuator parameters, an analytical model was formulated. This model is desirable as it aids in the understanding of the basic physics responsible for the transduction. It also minimizes optimization computational time and provides analytical scaling information. The solution for the actuator deflection due to an applied external voltage was obtained using piecewise-continuous solutions for the three regions of the actuator, namely, the gap region, the composite region, and the shim region.

Calculation of dc Response

As discussed in the preceding sections, the application of a voltage produces a couple that acts at the edges of the piezoelectric patch. The clamped-free composite beam is split into three (i.e., gap, composite, and shim) regions as shown in Fig. 2. The static Euler–Bernoulli [11] beam equation is solved in each region. The effects of transverse shear, rotary inertia, and geometric nonlinearities are neglected [12].

The deflection and slope are matched at the interface between regions. The result is that there is no deflection in the gap region, $w_1(x) = 0$, $0 \leq x < L_{\text{gap}}$, whereas the piecewise-continuous beam deflections in the other two regions are

$$w_2(x) = \frac{M_0}{(EI)_c}\left[\frac{x^2 + L_{\text{gap}}^2}{2} - L_{\text{gap}}x\right], \qquad L_{\text{gap}} \leq x < L_{\text{gap}} + L_p \qquad (4)$$

and

$$w_3(x) = \frac{M_0}{(EI)_c}(L_p)\left(x - L_{\text{gap}} - \frac{L_p}{2}\right), \qquad L_{\text{gap}} + L_p \leq x \leq L_T \qquad (5)$$

where $(EI)_c = E_s I_{s_2} + E_p I_{p_2}$ is an effective flexural rigidity in the composite region. The moment of inertia of the shim and the piezoelectric layer is denoted by I_{s_2} and I_{p_2}, respectively, and E_s is the elastic modulus of the shim. The preceding equations can be used to determine the quasi-static reciprocal relationship between the applied voltage and tip displacement. The ideal case neglects the size of the gap region by setting $L_{\text{gap}} \to 0$ so $x = L_T \cong L_p + L_s$. Substituting for M_0 and $(EI)_c$, the resulting tip deflection is

$$w_{\text{tip}} \cong \frac{3E_p t_s(t_s + t_p)E_s L_p(L_p - 2L_T)d_{31}V}{(E_s^2 t_s^4 + 4E_s t_s^3 E_p t_p + 6E_p t_p^2 E_s t_s^2 + 4E_p t_p^3 E_s t_s + E_p^2 t_p^4)} \qquad (6)$$

Defining nondimensional parameters $\bar{t} = t_p/t_s$, $\bar{L} = L_p/L_T$, $\xi = t_s/L_T$, and $\bar{E} = E_p/E_s$ leads to an expression for the nondimensional tip displacement

$$W = \frac{w_{\text{tip}}t_p}{d_{31}VL_T} \cong \frac{3\bar{E}(1 + \bar{t})\bar{t}(\bar{L} - 2)\bar{L}}{\xi(1 + 4\bar{E}\,\bar{t} + 6\bar{E}\bar{t}^2 + 4\bar{t}^3\bar{E} + \bar{E}^2\bar{t}^4)} \qquad (7)$$

Equation (7) gives the nondimensional tip deflection for a given piezoelectric material of a specified total length subject to an applied electric field. The design implications of the preceding expression will be discussed later in this paper. It can be shown that the dc response predicted by the analytical model is identical to that predicted by the perfect-bond model for an applied external voltage to the actuator with a negligible gap [13].

A similar analysis can be carried out for a symmetric bimorph actuator (Fig. 5). A bimorph actuator has oppositely poled piezoelectric patches attached to both sides of the shim and is used in applications that require greater displacement. For the bimorph, the induced moment at the interface between the piezoelectric patch and the shim is given by

$$M_b = -E_p t_p d_{31}E_{\text{field}}bt_s\left(\frac{t_p}{t_s} + 1\right) \qquad (8)$$

Following the same procedure as for the unimorph, the nondimensional tip deflection is

$$W = \frac{w_{\text{tip}}t_p}{d_{31}VL_T} \cong \frac{6\bar{E}(1 + \bar{t})\bar{t}(\bar{L} - 2)\bar{L}}{\xi(1 + 6\bar{E}\,\bar{t} + 12\bar{E}\bar{t}^2 + 8\bar{t}^3\bar{E})}$$
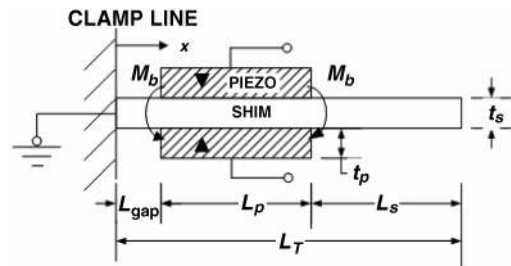

Fig. 5 Schematic of a bimorph actuator.

A comparison with Eq. (7) reveals that, when the denominator in either equation is approximately unity, the bimorph deflection is twice that of the unimorph.

Calculation of Natural Frequency

Following the lumped element modeling approach used in transducer design theory [14], the natural frequency of the composite beam is calculated based on the static tip deflection of the composite beam. To obtain the mode shape for the calculation of the lumped parameters, the beam is assumed to deflect under its own weight, and the corresponding Euler–Bernoulli beam equations are solved for the deflection due to the self-load $w_{sl}(x)$. The potential energy associated with the strain energy in the beam is given by [15]

$$U = \frac{1}{2} \int_0^{L_T} E(x) I(x) \left(\frac{d^2 w_{sl}(x)}{dx^2} \right)^2 dx \tag{10}$$

whereas the kinetic energy is given by [15]

$$T = \frac{1}{2} \int_0^{L_T} m_l(x) |\dot{w}_{sl}(x)|^2 dx \tag{11}$$

Here $m_l(x)$ is the mass per unit length of the actuator, and $E(x)$ and $I(x)$ are the elastic modulus and the moment of inertia, respectively. Assuming harmonic motion, $\dot{w}_{sl}(x) = dw_{sl}(x)/dt = i\omega w_{sl}(x)$, where ω is the angular frequency and $i = \sqrt{-1}$. Lumping the potential energy and the kinetic energy at the tip [14] provides an effective compliance

$$C_{\text{eff}} = \frac{[w_{sl}(L_T)]^2}{2U} \tag{12}$$

and effective mass

$$M_{\text{eff}} = \frac{2T/\omega^2}{[w_{sl}(L_T)]^2} \tag{13}$$

of the composite beam, respectively, where $w_{sl}(L_T)$ is the tip deflection. The fundamental resonant frequency of the composite beam is then estimated by

$$f_n = \frac{1}{2\pi} \sqrt{\frac{1}{C_{\text{eff}} M_{\text{eff}}}} \tag{14}$$

The general approach outlined in the preceding discussion applies to both a unimorph and bimorph actuator. The analytical expressions for $w_{sl}(L_T)$, U, and T are large and are provided in the Appendix. Finally, the natural frequency is normalized by that of a homogenous beam [15]

$$F = \frac{f_n}{0.1622} \sqrt{\frac{\rho_s L_T^4}{E_s t_s^2}} \tag{15}$$

It can be shown that F is a function of $\bar{t}$, $\bar{L}$, $\bar{E}$, and the density ratio $\bar{\rho} = \rho_p/\rho_s$ [13]. Note that the natural frequency is a measure of the bandwidth of the actuator and will be used later in this paper in the design optimization section.

Experimental Setup and Procedure

Experiments were conducted in the Interdisciplinary Microsystems Laboratory at the University of Florida to validate the preceding models by measuring the dc response and natural frequencies of various piezoelectric unimorph actuators.

The current work is an extension of a preliminary modeling and design study of piezoelectric actuators described in which a set of actuators were built and tested [10]. The dc response was predicted reasonably well by both finite element models, but there was a significant discrepancy between experimental and theoretical results for the natural frequencies, especially for large piezoelectric patch sizes ($\bar{L} > 0.5$). The reasons for the discrepancies included the

Table 2 Actuator dimensions

Property	Actuator design
Shim material	AL-2024
Piezoelectric material	PZT-5H
Bond material	Eccobond 45 epoxy
Total length	70 mm
Width	26 mm
Shim thickness	0.508 mm
Piezoelectric layer thickness	0.254 mm
Bond thickness	13–25 μm

uncertainty in actuator geometry and material properties, deviation from a clamped boundary condition, use of a low glass transition temperature epoxy adhesive for the bond layer, and nonuniformity of the bond layer thickness. All these issues were addressed and rectified in the present study, and the details are presented in Mathew [13].

Table 2 summarizes the actuator dimensions and materials. Note that the piezoelectric patch was bonded to the shim using Eccobond 45 epoxy adhesive [16]. Eccobond 45 is a good choice for the adhesive because it possesses a glass transition temperature of 48°C (ACX Technical data sheet [16]). A higher glass transition temperature ensures a stiffer bond and also reduces the dissipative losses. The measured thickness of the bond layer varied from 13–25 μm over the bonding area. Ten such actuators were constructed in which the nondimensional length of the piezoelectric patch $\bar{L}$ was varied from slight (10%) to full coverage (100%).

A schematic of the experimental setup used to characterize the actuator dynamic response is shown in Fig. 6. A periodic sweep excitation signal was generated using a function generator (HP model E1441A). The sweep signal spanned a frequency range from 0.1 to 200 Hz with amplitude of 0.05 V. The voltage signal was amplified by a nominal gain of 30 using an amplifier (PCB Model 790A06). The period of the signal was set at 4 s to provide good frequency resolution ($\Delta f = 0.25$ Hz) for the spectral analysis. The resulting data was acquired using a 16-bit data acquisition system (HP model E1433A). Fifty block averages of the spectral data were found suitable to reduce the random error component to acceptable levels. The beam from the laser displacement sensor (Micro-Epsilon Model ILD2000-10) was focused at a point approximately 1 mm from the midpoint of the tip of the actuator, and the frequency response function between the actuator output and the input voltage was measured. The dc response and the natural frequency were extracted from the resulting frequency response function.
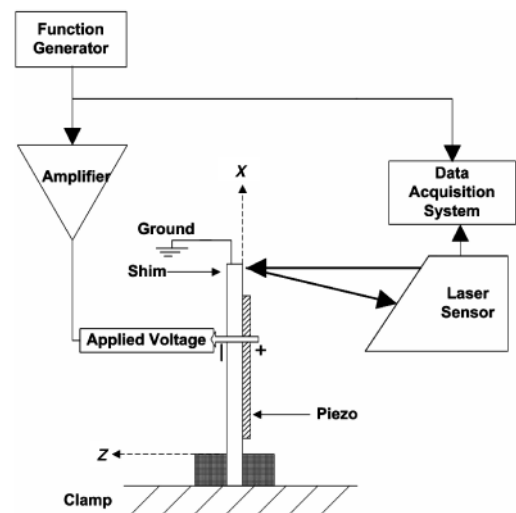

Fig. 6 Experimental setup with the laser displacement sensor.

There are a few experimental setup issues that are noteworthy. First, the dimension of the gap $L_{gap} \approx 1$ mm was selected to prevent arcing of the piezoelectric layer upon excitation by a large voltage and also to minimize the stress concentration on the piezoelectric layer. Second, to minimize the effect of anticlastic curvature upon bending, all measurements were made at the midpoint of the actuator tip, where both beam and plate theories behave identically, at least until the first bending mode [12]. Finally, to determine the effect of acoustic radiation mass loading [14], experiments were also conducted in a vacuum environment. There was no measurable effect on the frequency response function, indicating that the acoustic radiation mass is negligible for the tested conditions [13].

Results and Discussion

In this section, the experimental results are compared with values obtained from the two finite element models as well as the analytical model described in preceding sections. The resulting dc response and the natural frequency in all of the theoretical models are calculated using the nominal values of each variable. There are several ways to measure the dc response of the piezoelectric actuators. A static test to measure the tip deflection of the actuator with a constant external voltage can be used. However, a dynamic frequency response is an easier method because the dc response is given by the asymptotic limit of the frequency response at low frequency. Another estimate for the dc response can be obtained from a curve-fit to a second-order system model. As described in Mathew [13], all of these methods give essentially identical results that are well within the estimated experimental uncertainty of $\pm 15\%$. The average of the first 10 frequency response function magnitude values gives an estimate of the dc response. Another estimate for the dc response can be obtained from a second-order system model

$$H(s) = \frac{W_{tip}(s)}{V(s)} = \frac{1}{s^2 + 2\zeta\omega_n s + \omega_n^2} \qquad (16)$$

where the frequency response function, $H(s = j\omega)$, is defined as the ratio of the tip displacement $W_{tip}(s)$ to the applied voltage $V(s)$, for each angular frequency ω, and is a function of the natural frequency ω_n and damping ratio ζ. The natural frequency was calculated using various methods: the frequency corresponding to a 90 deg phase shift, the frequency corresponding to the peak of the power spectral density, a least-squares fit to Eq. (16), and an impact hammer test. Excellent agreement between all methods and repeatability was obtained. The details of these multiple methods for the calculation of dc response and natural frequency are provided in Mathew [13].
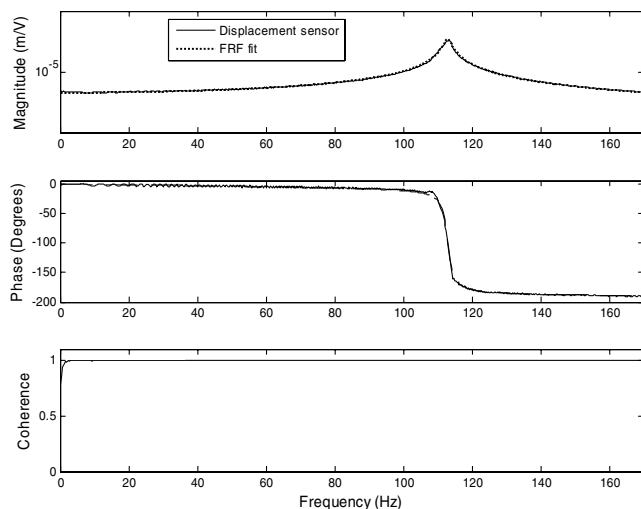

Fig. 7   Frequency response function magnitude, phase, and coherence for the actuator with $\bar{L} = 0.4$.
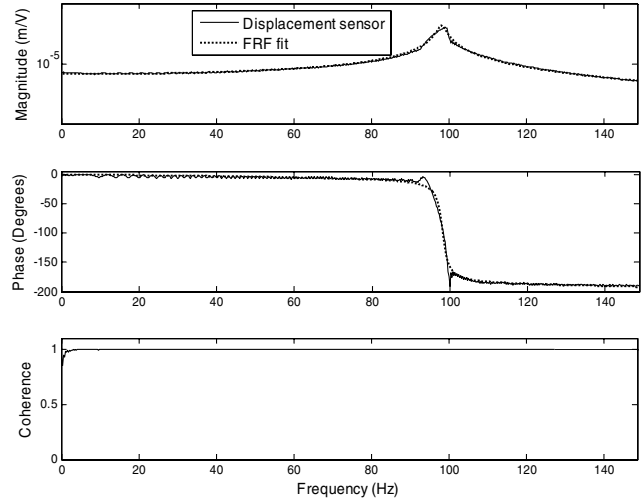

Fig. 8   Frequency response function magnitude, phase, and coherence for the actuator with $\bar{L} = 0.9$.

Figure 7 shows the frequency response function magnitude, phase, and coherence for the actuator with $\bar{L} = 0.4$. Also plotted on the same graph is the fit for the experimental frequency response, assuming the actuator to be a second-order underdamped system. As seen from the plot the natural frequency is approximately 114.5 Hz, and the dc response is 2.33×10^{-6} m/V. In the phase plot, the frequency where the phase crosses the 90 deg point is the natural frequency of the actuator. The frequency response function yields a coherence of almost unity over the whole range, except at very low frequencies. Figure 8 shows the response for an actuator with a larger piezoelectric patch, $\bar{L} = 0.9$. The natural frequency is approximately 98 Hz, and the dc response has increased to 4.99×10^{-6} m/V. The results also show that the system is devoid of nonlinearities, as indicated by the near unity coherence plots.

A comparison of the natural frequency of the actuators between theory and experiment is plotted versus $\bar{L}$ in Fig. 9. The experimental uncertainties are calculated from the frequency resolution in the frequency response measurements and the random error from repeating the experiment several times [13]. The experimental results agree well with the theory to within $\pm 10\%$. Theoretical values include predictions from the analytical model and the perfect-bond and shear-lag finite element models. As expected, the prediction from the shear-lag model is closest to the experimental values. The perfect-bond model predicts higher natural frequencies than the shear-lag model, whereas the analytical model serves as an upper limit for the theoretical predictions. Note that the analytical model gives identical results to the perfect-bond finite element model if $L_{gap} = 0$. A peak in the system bandwidth is observed for $\bar{L} \cong 0.5$. For low values of $\bar{L}$, increasing $\bar{L}$ has a greater impact on the stiffness
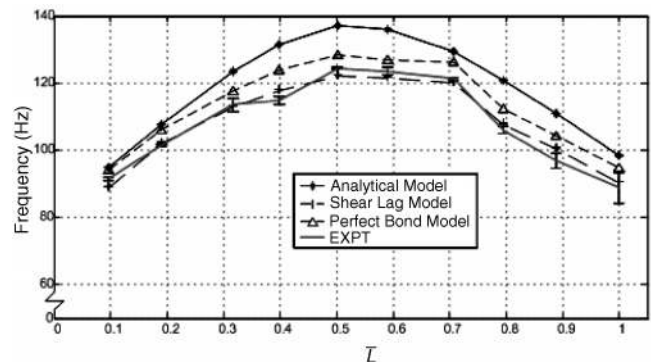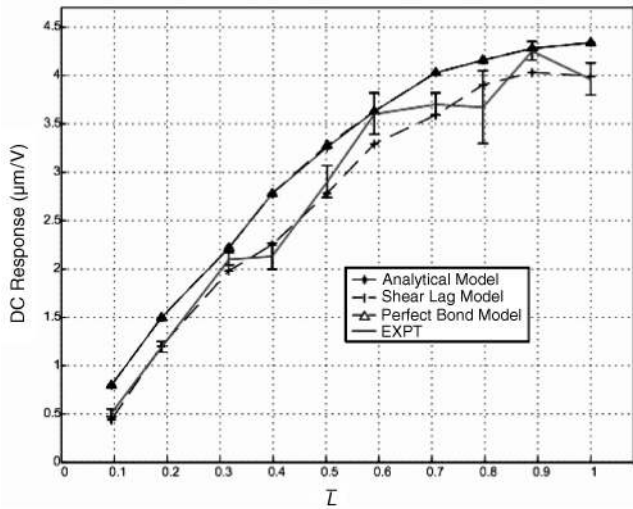

Fig. 9   Natural frequency variation with $\bar{L}$.

Fig. 10 Variation of dc response with $\bar{L}$.

than on the mass of the actuator. However, at higher values of $\bar{L}$, increasing $\bar{L}$ has a greater impact on the mass than on the stiffness of the actuator. Thus, there is a specific length $\bar{L}$ that balances these two competing effects. This provides insight into the optimum piezoelectric patch length for maximizing the natural frequency of the present piezoelectric actuator.

Figure 10 compares the dc response between theory and experiment. All models predict the dc response to a reasonable accuracy of ±15%. The dc response increases monotonically with increasing piezoelectric patch length and saturates around a value of $\bar{L} = 0.9$. It is intuitive that increasing the piezoelectric patch length induces more strain, which leads to larger tip displacements and hence a larger dc response. Thus, the experimental data presented here give confidence in the theoretical predictions by the models developed, with the shear-lag finite element model being the most accurate and the analytical model being the simplest.

Actuator Design Considerations

The experimental results suggest that the dc response increases monotonically with $\bar{L}$ while an optimum piezoelectric patch length exists that maximizes the system bandwidth. However, the study investigated the dependence of the dc response and the natural frequency of the actuator on only one parameter, $\bar{L}$. Yet the analytical model, described earlier, showed that the nondimensional dc response W also depends on $\bar{t}$, $\bar{E}$, and ξ. Similarly, the nondimensional natural frequency F is a function of $\bar{t}$, $\bar{L}$, $\bar{E}$, and $\bar{\rho}$.

A nominal "good" design corresponding to the actuator with the largest bandwidth with $\bar{L} = 0.5$, $\bar{t} = 0.5$, $\bar{E} = 0.85$, $\xi = 0.0073$, and $\bar{\rho} = 2.48$ is selected to study the sensitivity of both W and F on the actuator parameters. Figure 11 shows the variation of the ratio of nondimensional dc response to the nominal value of nondimensional dc response, W/W_{nominal}. For each plot only a single parameter is varied, while all other parameters are fixed at their nominal value. W increases monotonically with both modulus ratio, $\bar{E}$, and patch size, $\bar{L}$. Further, W increases initially as the thickness of the piezoelectric layer is increased until a value of $\bar{t} = 0.54$ and then decreases at higher values. Finally, W drops monotonically as ξ is increased. As shown in Fig. 12, the bimorph actuator exhibits similar behavior.

The variation of F with the design parameters for a unimorph is shown in Fig. 13. It can be seen that F increases with increasing stiffness ratio and thickness ratio but decreases with increasing density ratio. F peaks at a length ratio of $\bar{L} = 0.53$ and then decreases when the piezoelectric patch length is increased further. Again, similar behavior is exhibited by the bimorph in Fig. 14.

It is clear from the preceding plots that the actuator performance depends on a number of design parameters, and hence, a design optimization has to be performed to develop an actuator that provides the best performance. Because the analytical model gives identical results to the perfect-bond finite element model, if $L_{\text{gap}} = 0$, the optimization results for the analytical model are identical to the perfect-bond model in this case. Accounting for the finite gap size in the perfect-bond model and/or the shear lag will improve the accuracy of the natural frequency and dc response estimates at the cost of increased complexity associated with constructing and implementing these more complex models. Consider the example of one of the unimorph actuators developed that has a total length of

a) Stiffness ratio $\bar{E}$

b) Thickness ratio $\bar{t}$

c) Ratio of shim thickness to total actuator length ξ

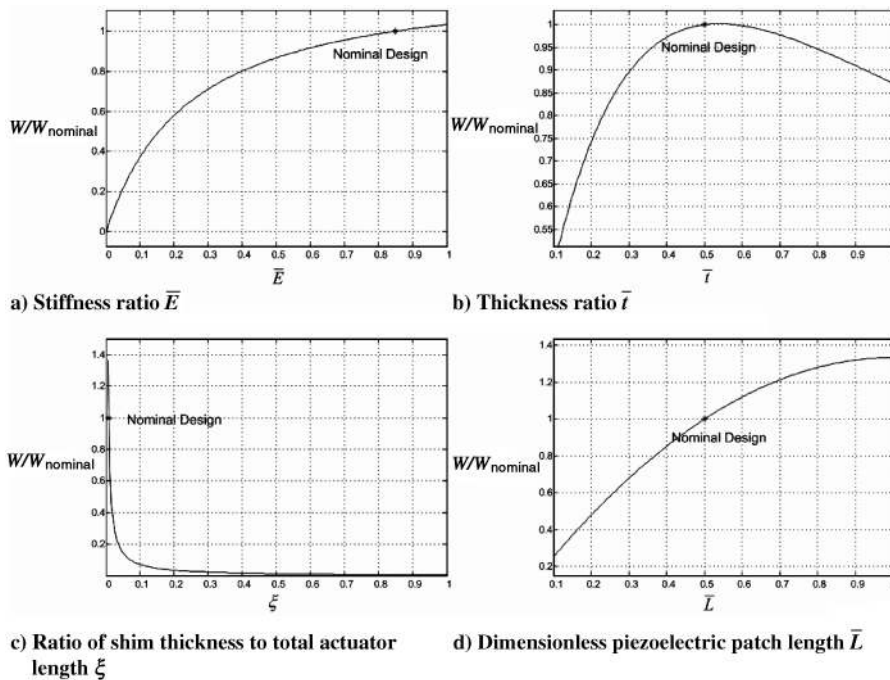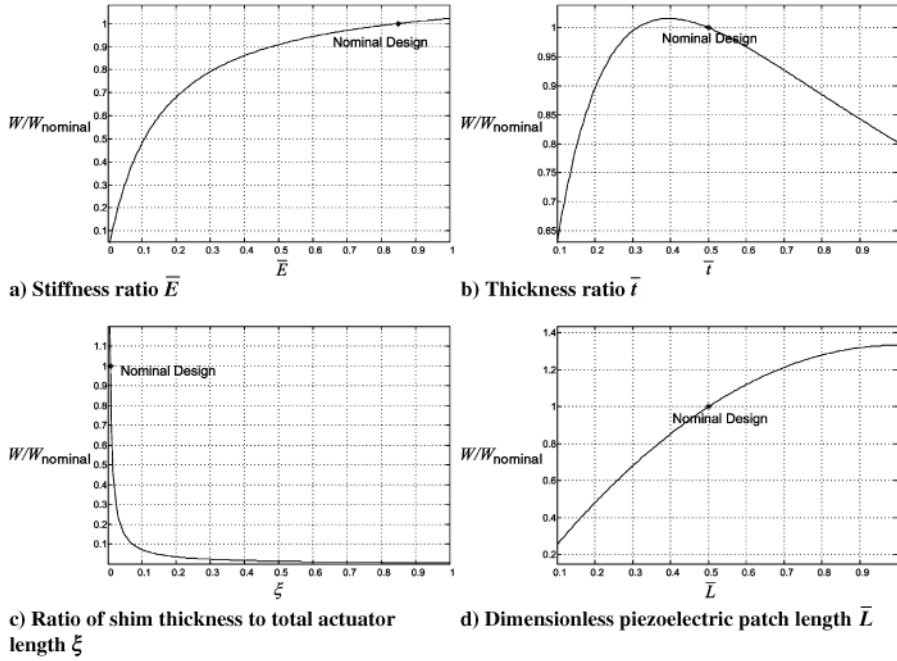d) Dimensionless piezoelectric patch length $\bar{L}$

Fig. 11 Variation of nondimensional dc response with the design parameters for a unimorph.

Fig. 12   Variation of nondimensional dc response with the design parameters for a bimorph.
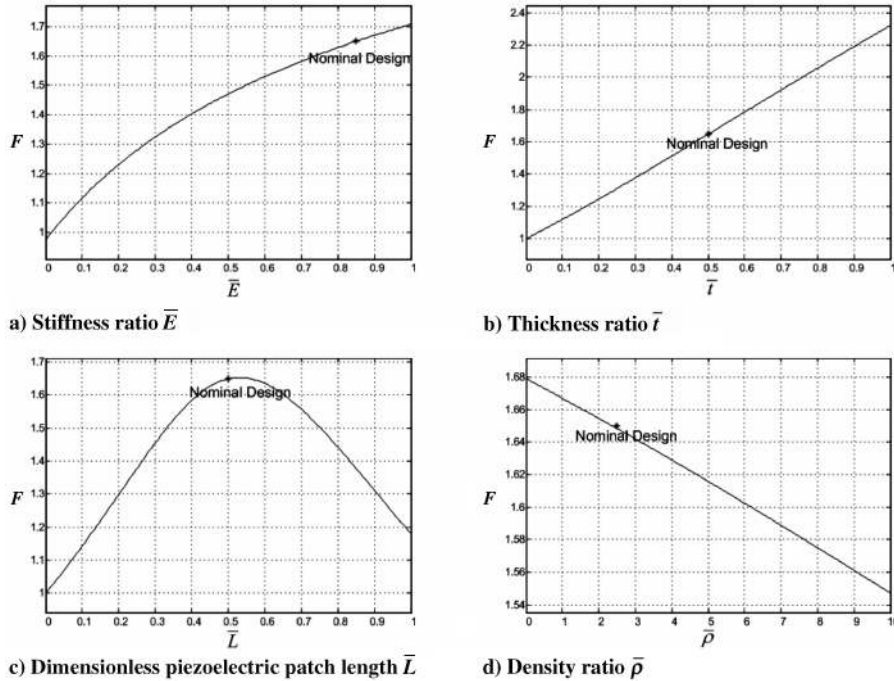
a) Stiffness ratio $\overline{E}$

b) Thickness ratio $\overline{t}$

c) Ratio of shim thickness to total actuator length ξ

d) Dimensionless piezoelectric patch length $\overline{L}$

Fig. 13   Variation of nondimensional natural frequency with the design parameters for a unimorph.

a) Stiffness ratio $\overline{E}$

b) Thickness ratio $\overline{t}$

c) Dimensionless piezoelectric patch length $\overline{L}$

d) Density ratio $\overline{\rho}$

70 mm and a piezoelectric patch length of 35 mm (Table 2). The natural frequency of this actuator calculated from the analytical model is 137 Hz, and its nondimensional dc response, W, is 44.2. For a unimorph actuator with a fixed L_T and specified materials subjected to a maximum applied electric field, we seek to maximize W by varying $\overline{t}$, $\overline{L}$, and ξ while maintaining a *minimum* value of the natural frequency at 137 Hz. We are also interested in estimating any increase in W that can be achieved using a similarly optimized bimorph actuator. A gradient descent method was used to minimize the cost function, $-W = -w_{\text{tip}} t_p / d_{31} V L_T$, subject to an inequality

constraint on the minimum actuator natural frequency and geometric size constraints [17].

To gain more insight into the choice of the cost function, let us examine the terms used in the definition of $-W$. The total length of the piezoelectric actuators L_T is a constant due to typical size constraints; the actuator cannot exceed a specified length. The maximum deflection is achieved when the value of the electric field equals the value of the coercive field of the piezoelectric material, which is approximately $V_{\max}/t_p \cong 30$ V/mil ($=1.18$ V/μm) for PZT-5H. Thus, the optimal choice corresponds to $V = V_{\max}$ that
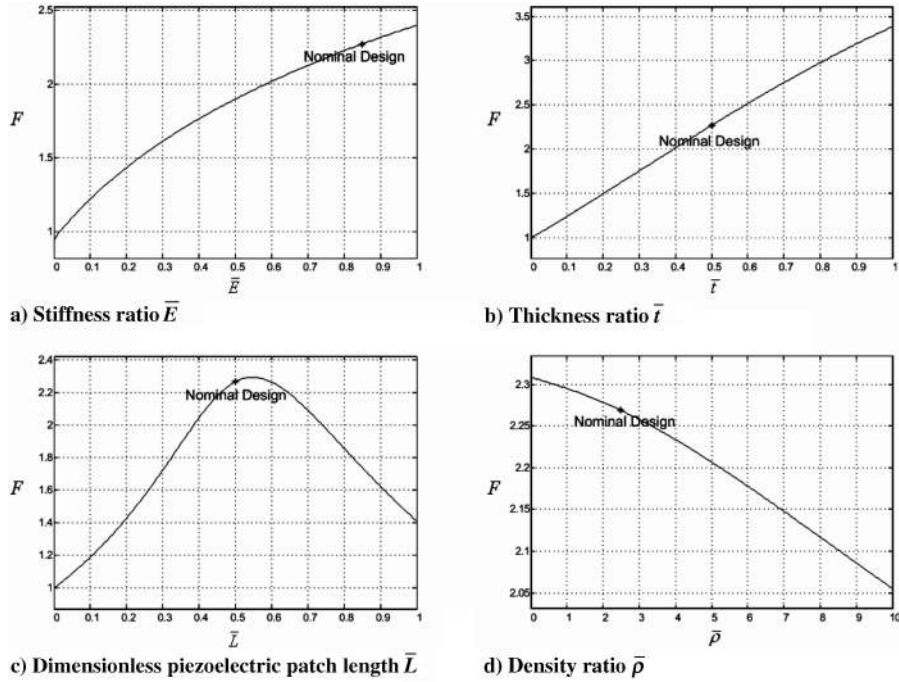
Fig. 14 Variation of nondimensional natural frequency with the design parameters for a bimorph.

corresponds to the coercive field strength. Note the analogy with an optimal sensor design, where the goal is to minimize the "minimum detectable signal" subject to electrical noise floor limitations. With an actuator, we seek the maximum achievable displacement subject to electric breakdown. Our experience indicates that electrical breakdown occurs before mechanical failure.

Both the cost function and the constraints are continuous and real valued. However, the gradient descent method may result in a local minimum. Therefore, two additional methods are used to increase the probability of finding the global minimum. First, several initial conditions are used within the domain of possible solutions. Then, the optimization function is used to find the local minima for each of these initial conditions, and the global optimum is selected. Next, a direct search method [18] is employed. This method searches for an optimal point and does not require any information about the gradient of the cost function.

The results of the optimization study are summarized in Table 3 and indicate that the optimized unimorph design has increased W by ∼43% compared with the nominal design while maintaining the same natural frequency. Furthermore, the value of W obtained from the optimized bimorph case is approximately twice that for the optimized unimorph. In practice, the sensitivity of the natural frequency, f_n, and the nondimensional tip deflection, W, to each of the design parameters is an important issue. Small variations in the design parameters, t_p, t_s, and L_p, should not cause large changes in the values for the natural frequency and tip deflection. A sensitivity study was therefore conducted in which each of the design parameters were varied by ±5% individually while keeping the two other parameters fixed, and the resulting values for the natural frequency and the nondimensional tip deflection were examined. The

results showed that the changes in the values for natural frequency and nondimensional tip deflection did not exceed 5%.

Thus, by constructing an actuator based on the optimized dimensions, maximum tip deflection can be achieved for a prescribed natural frequency. This result is of particular importance in flow-control applications, which makes use of large tip displacements of the actuator while placing constraints on the bandwidth of generation.

Effect of Fluid Loading on Piezoelectric Actuator

The effect of the flow on the output of the piezoelectric flap actuator is addressed in this section. A sample application of the flap actuator to control of separated flow from a backward-facing step was examined by Cattafesta et al. [7]. Their experimental data and scaling analysis shows that the ratio of the generated maximum velocity disturbance amplitude to the freestream velocity, $u'_{\max}/U_\infty \propto A_{\mathrm{tip}}\mathrm{Re}^{5/6}/\delta$, is strongly dependent on the actuator tip displacement and freestream velocity but only weakly dependent upon the boundary-layer thickness. Therefore, it appears that significant velocity fluctuation can be produced by this kind of oscillating flap.

Further validations of the aerodynamic loading experiments for these piezoelectric actuators in a wind-tunnel facility are given in Kegerise et al. [19] and Schaeffler et al. [20]. A flap-type piezoelectric bimorph actuator was designed based on the analytical model described in preceding sections. This actuator was installed in a wind-tunnel cavity model to suppress flow-induced cavity oscillations shown in Fig. 1d. Tip displacement measurements were made for three flow conditions at $M_\infty = 0.275, 0.4$, and 0.6 and also at the wind-off condition. The results of the actuator transfer functions for these conditions are provided in this reference and indicate that the flow has no measurable influence on the actuator dynamic response over the range of tested flow conditions. Therefore, the presence of parallel crossflow over the actuator surface has little influence on the dynamic response of the actuators.

Finally, based on the actuator design procedure discussed in preceding sections, a piezoelectric unimorph actuator was used for both open- and closed-loop control to suppress flow-induced cavity resonance, resulting in sound pressure level reductions in the cavity

Table 3 Optimization results

Parameter	Optimized unimorph	Optimized bimorph	Nominal design
L_T, mm	70	70	70
t_s, μm	312	99	508
t_p, μm	408	308	254
L_p, mm	44.7	46	35
f_n, Hz	137	137	137
W	62.8	127.3	44.2

of up to 20 dB [5]. Similar results are presented in Kegerise et al [19,21].

Conclusions

An analytical model and two finite element models, one based on the assumption of a perfect bond between the shim and the piezoelectric layer and the other based on the assumption of a finite shear lag between the shim and the piezoelectric patch, were developed and compared with tip displacement frequency response measurements of piezoelectric unimorph actuators. A parametric validation study was conducted in which the size of the piezoelectric patch was systematically varied from 10 to 100% of the entire beam length in approximately 10 equal steps (while all other variables were fixed).

The dc response and the natural frequency of the actuators were extracted from the frequency response function and compared with the models. Of the two finite element models, the shear-lag model gave better predictions than the perfect-bond model, as expected. All models predicted the dc response with reasonable accuracy (within $\pm 15\%$). The analytical natural frequency served as an upper limit for the theoretical predictions, the best estimate of which was again obtained by the shear-lag model.

The benefit of the analytical model is that it describes the functional dependence of the actuator bandwidth and dc response on the system parameters and predicts the response to a reasonable accuracy (within $\pm 10\%$). The finite element models have improved accuracy but at the expense of increased complexity and lack of physical insight concerning the dependence of the nondimensional dc response on $\bar{t}$, $\bar{L}$, $\bar{E}$, and ξ and the dependence of nondimensional natural frequency on $\bar{t}$, $\bar{L}$, $\bar{E}$, and $\bar{\rho}$. The analytical model was also extended to study the response of piezoelectric bimorph actuators.

As noted, the primary motivation for this study is to develop and validate design tools for piezoelectric flap actuators. An optimization study was carried out that addressed the dependence of actuator response on the critical actuator parameters involved. The nondimensional tip deflection was selected as the cost function for the optimization subject to a set of constraints on the dimensions of the actuator and the device bandwidth. The optimization scheme was also extended to bimorph actuators. The bimorph actuators were found to provide greater tip deflection than unimorph actuators for the same bandwidth, making them an ideal choice for large tip displacement applications in which electrical lead access on both sides is possible. The results provided an optimum design of the actuator that has the highest value for the nondimensional tip deflection for a prescribed bandwidth frequency.

Appendix

The tip deflection due to self-loading is

$$w_{\mathrm{sl}}(L_T) = \frac{[6q_3 L_p L_T^2(3L_p - 2L_T) + (L_p^4 - 4L_T L_p^3)(q_2 + 2q_3)]}{24(EI)_c}$$
$$- \frac{q_3(L_p - L_T)^4}{8(EI)_s} \tag{A1}$$

where $(EI)_s = E_s I_{s_3}$ and $q_2 = m_{l_2} g$ and $q_3 = m_{l_3} g$ are the weight per unit length of the composite and tip-region shim sections, respectively.

The potential energy associated with the deflection of the total piezoelectric beam is calculated from Eq. (10)

$$U = -\frac{q_3^2(L_p - L_T)^5}{40(EI)_s} + \frac{(-1/24q_2 q_3 + 1/24q_3^2 + 1/40q_2^2)L_p^5}{(EI)_c}$$
$$- \frac{q_3(2q_3 + q_2)L_T L_p^4}{24(EI)_c} + \frac{q_3(2q_3 + q_2)L_T^2 L_p^3}{12(EI)_c} - \frac{q_3^2 L_T^3 L_p^2}{4(EI)_c}$$
$$+ \frac{q_3^2 L_T^4 L_p}{8(EI)_c} \tag{A2}$$

Similarly, the kinetic energy is calculated from Eq. (11)

$$T = \omega^2 \Bigg\{ -\frac{m_{l_3} q_3^2 (L_p - L_T)^9}{500(EI)_s^2} + \frac{m_{l_3} q_3^2 L_p^9}{(EI)_s (EI)_c^2} \left[\frac{(EI)_c}{240} - \frac{(EI)_c q_2}{4320 q_3} \right.$$
$$\left. - \frac{(EI)_s}{288} + \frac{13(EI)_s m_{l_2} q_2^2}{6480 m_{l_3} q_3^2} + \frac{13(EI)_s m_{l_2}}{10080 m_{l_3}} + \frac{(EI)_s q_2}{288 q_3} \right.$$
$$\left. - \frac{7(EI)_s q_2^2}{3456 q_3^2} - \frac{43(EI)_s m_{l_2} q_2}{13440 m_{l_3} q_3} \right] - \frac{m_{l_3} q_3^2 L_T L_p^8}{(EI)_s (EI)_c^2} \left[\frac{7(EI)_c q_2}{1440 q_3} \right.$$
$$\left. + \frac{11(EI)_c}{360} - \frac{(EI)_s q_2}{144 q_3} + \frac{31(EI)_s m_{l_2} q_2}{8064 m_{l_3} q_3} - \frac{(EI)_s q_2^2}{1152 q_3^2} - \frac{(EI)_s}{96} \right.$$
$$\left. - \frac{(EI)_s m_{l_2}}{336 m_{l_3}} \right] + \frac{m_{l_3} q_3^2 L_T^2 L_p^7}{(EI)_s (EI)_c^2} \left[\frac{41(EI)_c}{360} + \frac{(EI)_c q_2}{36 q_3} - \frac{(EI)_s}{24} \right.$$
$$\left. - \frac{(EI)_s m_{l_2}}{280 m_{l_3}} + \frac{71(EI)_s m_{l_2} q_2}{10080 m_{l_3} q_3} - \frac{(EI)_s q_2^2}{288 q_3^2} - \frac{(EI)_s q_2}{36 q_3} \right]$$
$$- \frac{m_{l_3} q_3^2 L_T^3 L_p^6}{(EI)_s (EI)_c^2} \left[\frac{25(EI)_c q_2}{432 q_3} + \frac{11(EI)_c}{40} - \frac{(EI)_s q_2^2}{216 q_3^2} + \frac{(EI)_s m_{l_2}}{144 m_{l_3}} \right.$$
$$\left. - \frac{17(EI)_s}{144} - \frac{7(EI)_s q_2}{144 q_3} \right] + \frac{m_{l_3} q_3^2 L_T^4 L_p^5}{(EI)_s (EI)_c^2} \left[\frac{17(EI)_c q_2}{288 q_3} + \frac{4(EI)_c}{9} \right.$$
$$\left. - \frac{17(EI)_s q_2}{288 q_3} + \frac{(EI)_s m_{l_2}}{160 m_{l_3}} - \frac{19(EI)_s}{96} \right] - \frac{m_{l_3} q_3^2 L_T^5 L_p^4}{(EI)_s (EI)_c^2} \left[\frac{169(EI)_c}{360} \right.$$
$$\left. + \frac{43(EI)_c q_2}{1440 q_3} - \frac{(EI)_s q_2}{36 q_3} - \frac{7(EI)_s}{32} \right] + \frac{m_{l_3} q_3^2 L_T^6 L_p^3}{(EI)_s (EI)_c^2} \left[\frac{37(EI)_c}{120} \right.$$
$$\left. + \frac{13(EI)_c q_2}{2160 q_3} - \frac{7(EI)_s}{48} \right] - \frac{m_{l_3} q_3^2 L_T^7 L_p^2}{(EI)_s (EI)_c^2} \left[\frac{41(EI)_c}{360} - \frac{(EI)_s}{24} \right]$$
$$+ \frac{13 m_{l_3} q_3^2 L_T^8 L_p}{720(EI)_s (EI)_c} \Bigg\} \tag{A3}$$

Notice that Eqs. (A1–A3) are applicable to both unimorph and bimorph piezoelectric composite beams. Only the beam stiffness $(EI)_c$ and the mass per unit length m_{l_2} in the composite sections differ. Once $w_{\mathrm{sl}}(L_T)$, U, and T are obtained, Eqs. (12–14) can be used to calculate the natural frequency.

References

[1] Seifert, A., Eliahu, S., Greenblatt, D., and Wygnanski, I., "Use of Piezoelectric Actuators for Airfoil Separation Control," *AIAA Journal*, Vol. 36, No. 8, Aug. 1998, pp. 1535–1537.

[2] Jacobson, S. A., and Reynolds, W. C., "Active Control of Streamwise Vortices and Streaks in Boundary Layers," *Journal of Fluid Mechanics*, Vol. 360, No. 1, April 1998, pp. 179–211.

[3] Wiltse, J. M., and Glezer, A., "Manipulation of Free Shear Flows Using Piezoelectric Actuators," *Journal of Fluid Mechanics*, Vol. 249, April 1993, pp. 261–285.

[4] Wiltse, J. M., and Glezer, A., "Direct Excitation of Small-Scale Motions in Free Shear Flows," *Physics of Fluids*, Vol. 10, No. 8, Aug. 1998, pp. 2026–2036.

[5] Cattafesta, L. N., III, Garg, S., Choudhari, M., and Li, F., "Active Control of Flow-Induced Cavity Resonance," AIAA Paper 97-1804, June 1997.

[6] Crawley, E. F., and de Luis, J. D., "Use of Piezoelectric Actuators as Elements of Intelligent Structures," *AIAA Journal*, Vol. 25, No. 10, 1987, pp. 1373–1385.

[7] Cattafesta, L. N., III, Garg, S., and Shukla, D., "Development of Piezoelectric Actuators for Active Flow Control," *AIAA Journal*, Vol. 39, No. 8, Aug. 2001, pp. 1562–1568.

[8] Cattafesta, L., Mathew, J., and Kurdila, A., "Modeling and Design of Piezoelectric Actuators for Fluid Flow Control," *SAE 2000 Transactions: Journal of Aerospace*, Vol. 109, No. 1, 2001, pp. 1088–1095.

[9] Rosan, S. L., *Fundamental Principles of Polymeric Materials*, 2nd ed., Wiley, New York, 1993, Chap. 18, pp. 298–350.

[10] Mathew, J., Sankar, B. V., and Cattafesta, L. N., III., "Finite Element Modeling of Piezoelectric Actuators for Active Flow Control Applications," AIAA Paper 2001-300, Jan. 2001.

[11] Timoshenko, S., and Young, D. H., *Elements of Strength of Materials*, 4th ed., Van Nostrand Company, Princeton, NJ, 1962, pp. 111–117.

[12] Reddy, J. N., *Mechanics of Laminated Composite Plates*, CRC Press, Boca Raton, FL, 1997, Chap. 2, pp. 81–108.

[13] Mathew, J., "A Theoretical and Experimental Study of Piezoelectric Unimorph Actuators for Active Flow Control," M.S. Thesis, University of Florida, Gainesville, FL, May 2002.

[14] Merhaut, J., *Theory of Electroacoustics*, McGraw–Hill, New York, 1981, Chap. 2, pp. 98–108.

[15] Thomson, W. T., *Theory of Vibration with Applications*, 4th ed., Prentice–Hall, Englewood Cliffs, NJ, 1993.

[16] "ACX Technical Data Sheet," Active Control eXperts, Cambridge, MA, 2001.

[17] Coleman, T. F., and Li, Y., "An Interior Trust Region Approach for Nonlinear Minimization Subject to Bounds," *SIAM Journal on Optimization*, Vol. 6, No. 2, May 1996, pp. 418–445.

[18] Torczon, V., "On the Convergence of Pattern Search Algorithms," *SIAM Journal on Optimization*, Vol. 7, No. 1, 1997, pp. 1–25.

[19] Kegerise, M. A., Cattafesta, L. N., and Ha, C., "Adaptive Identification and Control of Flow-Induced Cavity Oscillations," AIAA Paper 2002-3158, June 2002.

[20] Schaeffler, N. W., Hepner, T. E., Jones, G. S., and Kegerise, M. A., "Overview of Active Flow Control Actuator Development at NASA Langley Research Center," AIAA Paper 2002-3159, June 2002.

[21] Kegerise, M., Cabell, R. H., and Cattafesta, L. N., "Real-Time Adaptive Control of Flow-Induced Cavity Tones," AIAA Paper 2004-0572, Jan. 2004.

K. Shivakumar
Associate Editor